Micropropulsion and microrheology in complex fluids via symmetry breaking

On Shun Pak,[1] LaiLai Zhu,[2] Luca Brandt,[2,a)] and Eric Lauga[1,b)]
[1]*Department of Mechanical and Aerospace Engineering, University of California, San Diego, 9500 Gilman Drive, La Jolla, California 92093-0411, USA*
[2]*Linné Flow Center, KTH Mechanics, S-100 44 Stockholm, Sweden*

Many biological fluids have polymeric microstructures and display non-Newtonian rheology. We take advantage of such nonlinear fluid behavior and combine it with geometrical symmetry-breaking to design a novel small-scale propeller able to move only in complex fluids. Its propulsion characteristics are explored numerically in an Oldroyd-B fluid for finite Deborah numbers while the small Deborah number limit is investigated analytically using a second-order fluid model. We then derive expressions relating the propulsion speed to the rheological properties of the complex fluid, allowing thus to infer the normal stress coefficients in the fluid from the locomotion of the propeller. Our simple mechanism can therefore be used either as a non-Newtonian micro-propeller or as a micro-rheometer. © *2012 American Institute of Physics*. [http://dx.doi.org/10.1063/1.4758811]

I. INTRODUCTION

Life at low Reynolds numbers has attracted considerable attention in the past few decades.[1–4] The absence of inertia plays a remarkable role in the swimming of microorganisms. In a Newtonian flow, the scallop theorem[1] constrains the types of locomotion strategies which are effective in the microscopic world and reciprocal motion—as are called those with a time-reversal symmetry—cannot lead to any net propulsion (or fluid transport). Microorganisms evolved different propulsion strategies to achieve micro-propulsion, including the active propagation of flagellar waves for eukaryotic cells and the passive rotation of rigid helical flagella for bacteria.[2]

The physics of low Reynolds number locomotion is relatively well explored in the Newtonian limit (see reviews in Refs. 1–4 and references therein). Beyond improving our understanding of biological processes, applications of these physical principles led to progress in the design of synthetic micro-swimmers for potential future biomedical applications.[4–8] In contrast, fundamental properties of life in complex, non-Newtonian, flows remain surprisingly unaddressed. Non-Newtonian flow behaviors can be appreciated through well-known manifestations from daily life, for example, the climbing of dough up kitchen mixing blades (termed rod-climbing, or Weissenberg, effect) or the remarkable behavior of Silly Putty, a popular toy which bounces like a solid rubber ball when thrown to the floor but melts like a fluid when left on a surface for some time.[9–11]

Many situations exist wherein microorganisms encounter biological fluids which have polymeric microstructures and non-Newtonian rheological properties. For example, spermatozoa swim through the viscoelastic cervical mucus and along the mucus-covered fallopian tubes;[3,12–16] cilia lie in a layer of mucus along the human respiratory tract;[17] *Helicobacter pylori*, a bacterium causing ulcer, locomotes through mucus lining of the stomach;[18] spirochetes move through host tissue during infection;[19] in biofilms, bacteria are embedded in cross-linked polymer gels.[20–24]

a)Electronic mail: luca@mech.kth.se.
b)Electronic mail: elauga@ucsd.edu.

Physically and mathematically, the presence of polymeric stresses in a complex fluid means that the usual properties associated with the absence of inertia in the Newtonian limit cease to be valid, in particular, kinematic reversibility and the linearity of the flow equations. In return, non-Newtonian effects such as stress relaxation, normal stress differences, and shear-rate dependent viscosity manifest themselves.[9–11,25]

Past theoretical and experimental studies have investigated the waveforms and swimming paths of microorganisms in complex fluids.[3,4,12–15,26–28] An active discussion in the biomechanics community has recently focused on the simple question: Does fluid elasticity enhance or deteriorate propulsion at the microscopic scale? Theoretical studies on infinite models[29–31] showed that, for fixed body-frame kinematics, the propulsion speed decreases in a viscoelastic fluid. Numerical studies on a finite swimmer[32] demonstrated that the propulsion speed could be enhanced by the presence of polymeric stress for some prescribed kinematics. Experimental investigations suggested evidences for both.[33,34] It was also shown that reciprocal actuation on a fluid, unable to provide net locomotion or flow transport in the Newtonian case, can be rendered effective by viscoelasticity.[35–37] The presence of polymeric stress has also interesting consequences on the rate of flagellar synchronization.[38]

Normal stress differences in a complex fluid are responsible for a number of important non-Newtonian effects[9–11] including the rob-climbing effect mentioned above impacting many applications such as mixing, and the swelling of polymer melts when extruded from dies in manufacturing processes posing constraints on the rate of extrusion. In a pure shear flow with an arbitrary Reynolds number and a shear rate $\dot{\gamma}$, assuming that the flow is in the x-direction and the velocity varies in the y-direction, the z-direction being called the neutral direction,[9] the first and second normal stress coefficients are defined as $\Psi_1 = (\tau_{xx} - \tau_{yy})/\dot{\gamma}^2$ and $\Psi_2 = (\tau_{yy} - \tau_{zz})/\dot{\gamma}^2$, respectively, where τ_{ij} are the components of the deviatoric stress tensor. In a Newtonian flow, there are no normal stress differences ($\Psi_1 = \Psi_2 = 0$), whereas for polymeric fluids typically $\Psi_1 > 0$ and $\Psi_2 < 0$. The magnitude of the second normal stress coefficient is usually much smaller than that of the first normal stress coefficient ($|\Psi_2| \ll \Psi_1$). In the rob-climbing phenomenon, both first and second normal stress coefficients contribute to the effect.[9] However, due to its small magnitude, the effect of the second normal stress coefficient is shadowed by that of the first normal stress difference.[9] The existence of the second normal stress difference can be demonstrated in a free-surface flow driven by gravity through a tilted trough: a Newtonian fluid has a flat free surface (with negligible meniscus effect), while the free surface of a non-Newtonian fluid becomes convex due to second normal stresses.[39–41]

In this work, we propose a simple mechanism able to take advantage of the presence of normal stress differences to propel in a complex fluid. Our geometry, shown in Fig. 1, consists of two linked small spheres propelling under the action of an external torque, a setup we will refer to as a "snowman." Locomotion is enabled solely by the presence of normal stress differences, and no motion exists in a Newtonian environment, a fact that can in turn be used to infer the normal stress coefficients of a complex fluid. In essence, as complex fluids lead to new modes of small-scale propulsion, symmetrically the presence of propulsion in an environment can be used to locally probe the rheological properties of the fluid.

The first normal stress coefficient of a fluid can be measured directly from a conventional cone-and-plate rheometer;[9–11] the measurement of the second normal stress coefficient however has been a longstanding challenge.[42–45] A number of methods were proposed (see a review in Ref. 45), including a modified cone-and-plate rheometry with pressure transducers,[9,43] a subtle evaluation of a combination of cone-and-plate and parallel-plate experiments,[42] rheo-optical measurements,[42,44] and the use of a cone-and-partitioned plate tool.[45] Recently, a microrheological technique was proposed to measure the first and second normal stress coefficients.[46] In microrheology, colloidal probes are either actively driven, or passively diffusing, and their dynamics allows to infer local rheological information. Microrheology enjoys many advantages over conventional macroscopic rheological measurements,[47,48] including the reduction in sample size, the ability to probe spatially inhomogeneous environments, and the possibility of performing measurements in living cells.[47–50] The mechanism we propose in this paper would be classified as "active" microrheology, a situation where colloidal probes are actively manipulated to drive the material out of equilibrium and probe its nonlinear mechanical properties.[47,51] We offer in this paper an alternative microrheological technique capable of probing both first and second stress coefficients by using only kinematic measurements.
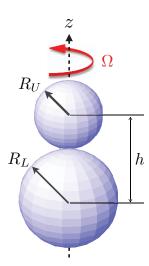
FIG. 1. Geometrical setup of two spheres ("snowman") rotating with angular velocity Ω along their separation axis. The radii of the upper and lower spheres are denoted by R_U and R_L, respectively. The centers of the spheres are separated by a distance, h (for touching spheres, $h = R_U + R_L$).

This paper is organized as follows. In Sec. II, we introduce the geometric and kinematic setup of our proposed mechanism and the polymeric fluid models adopted in our study. We first investigate in Sec. III the propulsion characteristics of the snowman in a complex fluid, followed in Sec. IV by the method of inferring the normal stress coefficients from its locomotion. We then provide a qualitative, and intuitive, explanation of the locomotion enabled by normal stresses in Sec. V before concluding the paper in Sec. VI.

II. SETUP

A. Kinematics

By symmetry, the rotation of a single sphere in any homogeneous fluid produces no net locomotion. Inserting a second sphere, of different size, breaks the geometrical symmetry and can potentially allow locomotion. We first consider the rotation of two unequal spheres touching each other as a single rigid body (see the geometry and notations in Fig. 1), the "snowman" geometry. We label the line of centers of the spheres as the z-axis. Without loss of generality, we assume the radius of the upper sphere (R_U) is smaller than that of the lower sphere ($R_L \geq R_U$). The distance between the centers of the spheres is denoted by h. For the case of touching spheres, we thus have $h = R_U + R_L$.

From a kinematic standpoint we assume that the rigid body rotates with a steady angular velocity about the z-axis, $\boldsymbol{\Omega} = (0, 0, \Omega > 0)$, but is otherwise free to move. Given that the snowman is axisymmetric, the only direction it could potentially move is the z-direction. We assume the net hydrodynamic force acting on the snowman is zero for all times (free-swimming condition), and aim at computing the rigid body (swimming) velocity necessary to maintain force-free motion.

In a Newtonian fluid without inertia, it is straightforward to show using kinematic reversibility and reflection symmetry that a rotating snowman cannot swim—a result true for any degree of geometrical asymmetry. The central question at the heart of this paper is: Can elasticity of the fluid enable propulsion of the snowman? We answer this question by studying the locomotion of a rotating snowman in polymeric fluids described by the two constitutive relations introduced below (Sec. II B).

B. Polymeric fluid dynamics

We consider an incompressible low-Reynolds-number flow in a complex fluid. Denoting the velocity field as $\mathbf{u}$ and the fluid stress as $\boldsymbol{\sigma} = -p\mathbf{I} + \boldsymbol{\tau}$, where p is the pressure, and $\boldsymbol{\tau}$ is the deviatoric stress tensor, the conservation of mass and momentum are given by the continuity equation and Cauchy's equation of motion, respectively,

$$\nabla \cdot \mathbf{u} = 0, \tag{1}$$

$$\nabla \cdot \boldsymbol{\sigma} = \mathbf{0}. \tag{2}$$

For closure, we require a constitutive equation relating the deviatoric stresses $\boldsymbol{\tau}$ to the kinematics of the flow. Obviously a large number of models have been proposed in the past to describe polymeric fluids. In this work two constitutive equations are used to study the viscoelastic locomotion of a snowman.

1. Oldroyd-B fluid

The classical Oldroyd-B constitutive equation is arguably the most famous constitutive model for polymeric fluids.[9–11,25] It has a sound physical origin and can be derived from a kinetic theory of polymers in the dilute limit by modeling polymeric molecules as linearly elastic dumbbells. The predictions also agree well with experimental measurements up to order one Weissenberg numbers, although it is known to suffer deficiencies for larger values.[9–11,25] In an Oldroyd-B fluid, the deviatoric stress is the sum of two components, $\boldsymbol{\tau} = \boldsymbol{\tau}^s + \boldsymbol{\tau}^p$, where $\boldsymbol{\tau}^s$ and $\boldsymbol{\tau}^p$ denote, respectively, the Newtonian solvent contribution and polymeric contribution to the stress. The constitutive relation for the Newtonian contribution is given by $\boldsymbol{\tau}^s = \eta_s \dot{\boldsymbol{\gamma}}$, where $\dot{\boldsymbol{\gamma}} = \nabla \mathbf{u} + \nabla \mathbf{u}^T$ is the rate of strain tensor and η_s is the solvent contribution to the viscosity. The momentum equation can thus be written as

$$-\nabla p + \eta_s \nabla \cdot \dot{\boldsymbol{\gamma}} + \nabla \cdot \boldsymbol{\tau}^p = \mathbf{0}. \tag{3}$$

The polymeric stress $\boldsymbol{\tau}^p$ is then assumed to be governed by the upper-convected Maxwell equation:

$$\boldsymbol{\tau}^p + \lambda \stackrel{\triangledown}{\boldsymbol{\tau}^p} = \eta_p \dot{\boldsymbol{\gamma}}, \tag{4}$$

where λ is the polymeric relaxation time and η_p is the polymer contribution to the viscosity.[9–11] The upper-convected derivative for a tensor $\mathbf{A}$ is defined as

$$\stackrel{\triangledown}{\mathbf{A}} = \frac{\partial \mathbf{A}}{\partial t} + \mathbf{u} \cdot \nabla \mathbf{A} - (\nabla \mathbf{u}^T \cdot \mathbf{A} + \mathbf{A} \cdot \nabla \mathbf{u}), \tag{5}$$

which calculates the rate of change of $\mathbf{A}$ while translating and deforming with the fluid.

Combining the Newtonian and polymeric constitutive relations, we obtain the Oldroyd-B constitutive equation for the total stress, $\boldsymbol{\tau}$, as

$$\boldsymbol{\tau} + \lambda \stackrel{\triangledown}{\boldsymbol{\tau}} = \eta(\dot{\boldsymbol{\gamma}} + \lambda_2 \stackrel{\triangledown}{\dot{\boldsymbol{\gamma}}}), \tag{6}$$

where the total viscosity is given by $\eta = \eta_s + \eta_p$, and $\lambda_2 = \lambda \zeta$ denote the retardation times (we define the relative viscosity $\zeta = \eta_s/\eta < 1$). For steady shear of an Oldroyd-B fluid, both the viscosity and the first normal stress coefficient are constant, and the second normal stress coefficient is zero.[9] The Oldroyd-B fluid is the model we will use for our numerical approach.

2. Second-order fluid

For slow and slowly varying flows, the second-order fluid model applies. It is the first non-Newtonian term in a systematic asymptotic expansion of the relationship between the stress and the rate of strain tensors called the retarded-motion expansion. It describes small departures from

Newtonian fluid behavior, and the instantaneous constitutive equation is given in this model by

$$\boldsymbol{\tau} = \eta\dot{\boldsymbol{\gamma}} - \frac{1}{2}\Psi_1\overset{\triangledown}{\dot{\boldsymbol{\gamma}}} + \Psi_2(\dot{\boldsymbol{\gamma}} \cdot \dot{\boldsymbol{\gamma}}), \tag{7}$$

where Ψ_1 and Ψ_2 are the first and second normal stress coefficients, respectively. Note that if $\lambda = 0$ while $\lambda_2 \neq 0$ in the Oldroyd-B model, Eq. (6), it reduces to a second-order fluid with a vanishing second normal stress coefficient ($\Psi_2 = 0$).[9] The second-order fluid model will enable us to derive theoretically the behavior of the snowman for small deformations.

C. Non-dimensionalization

We non-dimensionalize lengths by the radius of the lower sphere R_L, times by $1/\Omega$, and use the total fluid viscosity, η, to provide the third fundamental unit. Hence, velocities, shear rates, and stresses are scaled by $R_L\Omega$, Ω, and $\eta\Omega$, respectively. The dimensionless radius of the upper sphere becomes then $r^* = R_U/R_L$ while the lower sphere has now radius 1. We have $h^* = h/R_L$ denoting the dimensionless distance between the centers of the sphere ($h^* = 1 + r^*$ for two touching spheres). Both spheres rotate at the same dimensionless unit speed, $\Omega^* = 1$. The starred variables represent dimensionless variables in this paper. The Deborah number,[9–11] De $= \lambda\Omega$, is a dimensionless number defined as the ratio of a characteristic time scale of the fluid (the polymeric relaxation time, λ) to a characteristic time scale of the flow system ($1/\Omega$), and appears in the dimensionless momentum equation and upper-convected Maxwell equation:

$$-\boldsymbol{\nabla} p^* + \zeta\boldsymbol{\nabla} \cdot \dot{\boldsymbol{\gamma}}^* + \boldsymbol{\nabla} \cdot \boldsymbol{\tau}^{p*} = \mathbf{0}, \tag{8}$$

$$\boldsymbol{\tau}^{p*} + \text{De }\overset{\triangledown}{\boldsymbol{\tau}^{p*}} = (1 - \zeta)\dot{\boldsymbol{\gamma}}^*. \tag{9}$$

The limit De $= 0$ corresponds to a Newtonian fluid.

Alternatively, the upper-convected Maxwell equation of the polymeric stress, Eq. (9), can be combined with the constitutive relation of the Newtonian contribution to obtain the dimensionless Oldroyd-B constitutive equation for the total stress $\boldsymbol{\tau}^*$ as

$$\boldsymbol{\tau}^* + \text{De }\overset{\triangledown}{\boldsymbol{\tau}^*} = \dot{\boldsymbol{\gamma}}^* + \text{De}_2 \overset{\triangledown}{\dot{\boldsymbol{\gamma}}^*}, \tag{10}$$

where we have defined another Deborah number, De_2, in terms of the retardation time, $\text{De}_2 = \lambda_2\Omega = \text{De}\zeta$.

The dimensionless constitutive relation for a second-order fluid is now given by

$$\boldsymbol{\tau}^* = \dot{\boldsymbol{\gamma}}^* - \text{De}_{\text{so}}\left(\overset{\triangledown}{\dot{\boldsymbol{\gamma}}^*} + B\dot{\boldsymbol{\gamma}}^* \cdot \dot{\boldsymbol{\gamma}}^*\right), \tag{11}$$

where we have defined a different Deborah number for the second-order fluid, namely $\text{De}_{\text{so}} = \Psi_1\Omega/2\eta$, and $B = -2\Psi_2/\Psi_1 \geq 0$.

Importantly, we note that the definition of the Deborah number of an Oldroyd-B fluid is different from that of a second-order fluid, because the relaxation time of an Oldroyd-B fluid is defined only by the polymer, whereas the relaxation time of a second-order is defined by both the polymer and the solvent.[52] The two Deborah numbers are related by the relation $\text{De}_{\text{so}} = \text{De}(1 - \zeta)$. We shall mostly use the Deborah number defined for an Oldroyd-B fluid (De) for the presentation of our final results, since we feel it is the one with the most intuitive definition. The Oldroyd-B equation is valid up to moderate De, and the second-order fluid is valid for small De (or De_{so}), and we thus expect the results from both models to match when De (or De_{so}) is sufficiently small.

III. PROPULSION OF SNOWMAN IN A COMPLEX FLUID

As argued in Sec. II A, asymmetry alone does not lead to net locomotion upon rotating a snowman in a Newtonian fluid. We now explore the effects of fluid elasticity on the propulsion of a snowman: Does it even move? Which direction does it go? And how fast? Using the Oldroyd-B

fluid model, we first explore numerically the propulsion characteristics of the snowman from small to moderate Deborah numbers. Next, the small De limit is studied analytically via the second-order fluid model.

A. Moderate Deborah number

We employed a finite element model to compute the polymeric flow as described by Eqs. (8) and (9). A formulation called the discrete elastic-viscous split stress (DEVSS-G)[53,54] is implemented here to improve numerical stability. The momentum equation, Eq. (8), is rewritten as

$$\nabla \cdot \mu_a (\nabla \mathbf{u}^* + \nabla \mathbf{u}^{*T}) - \nabla p^* + \nabla \cdot \boldsymbol{\tau}^{p*} - \nabla \cdot (\mu_a - \zeta)(\mathbf{G} + \mathbf{G}^T) = \mathbf{0}, \quad (12)$$

where the tensor $\mathbf{G} \equiv \nabla \mathbf{u}^*$ is introduced as a finite element approximation of the velocity gradient tensor $\nabla \mathbf{u}^*$. An additional elliptic term, $\nabla \cdot \mu_a (\nabla \mathbf{u}^* + \nabla \mathbf{u}^{*T}) - \nabla \cdot \mu_a (\mathbf{G} + \mathbf{G}^T)$, is added into the momentum equation for stabilization.[55] In the limit that the mesh size in the finite element approximation tends to zero, $\mathbf{G}$ approaches $\nabla \mathbf{u}^*$ and the elliptic term vanishes, reducing Eq. (12) to Eq. (8). $\mathbf{G}$ is also used to approximate the velocity gradient term $\nabla \mathbf{u}^*$ in the constitutive equation, Eq. (9). For simulations in this work, we choose $\mu_a = 1$ as in Liu *et al.*[54]

A Galerkin method is used to discretize the momentum equations, continuity equation, and the equation for the additional unknown $\mathbf{G}$. Quadratic elements are used for $\mathbf{u}^*$ and linear elements for both p^* and $\mathbf{G}$. The streamline-upwind/Petrov-Galerkin (SUPG)[56] method is adopted to discretize the constitutive equation, Eq. (9), to improve numerical stability. The resulting weak form of the model is formulated as

$$\left\{ \mathbf{S} + \frac{h_c}{U_c} \mathbf{u}^* \cdot \nabla \mathbf{S}, \ \boldsymbol{\tau}^{p*} + \mathrm{De}(\mathbf{u}^* \cdot \nabla \boldsymbol{\tau}^{p*} - \mathbf{G}^T \cdot \boldsymbol{\tau}^{p*} - \boldsymbol{\tau}^{p*} \cdot \mathbf{G}) - (1 - \zeta)(\mathbf{G} + \mathbf{G}^T) \right\} = 0, \quad (13)$$

where $\mathbf{S}$ denotes the test function for $\boldsymbol{\tau}^{p*}$, h_c is a characteristic mesh size, and U_c is the magnitude of a local characteristic velocity (we choose the norm of $\mathbf{u}^*$ as U_c). The framework for the implementation is provided by the commercial software COMSOL, which was successfully used to simulate the locomotion of squirmers in a viscoelastic fluid at low Reynolds numbers.[57]

We perform three-dimensional axisymmetric simulations on a two-dimensional mesh constructed with triangle elements. Sufficiently refined mesh is generated near rotating objects to resolve the thin stress boundary layers, necessary to overcome numerical instabilities[58,59] and improve accuracy. We validate our implementation by comparing numerical and analytical values of the hydrodynamic torque on a rotating sphere in the Newtonian fluid. For the viscoelastic model, we validate our approach against the simulations in Lunsmann *et al.*[60] of a sedimenting sphere in a tube filled with Oldroyd-B fluid and the analytical results in Bird *et al.*[9] of a rotating sphere in a second-order fluid.

Equipped with our computational model, we are able to show that fluid elasticity does indeed enable the propulsion of the snowman provided the two spheres have unequal sizes ($r^* < 1$). The snowman always swims in the positive *z*-direction (see Fig. 1), i.e., from the larger to the smaller sphere. For illustration, we compute the dimensionless propulsion speed, $U^* = U/R_L\Omega$, of a typical snowman ($r^* = R_U/R_L = 0.5$) as a function of the Deborah number, De (red dots and dashed line, Fig. 2), for a fixed relative viscosity $\zeta = 0.5$. When De $= 0$, the fluid reduces to the Newtonian limit and we recover that no propulsion is possible in this case. For small values of De, the propulsion speed appears to grow linearly with De, a result confirmed analytically in Sec. III B. A maximum swimming speed is reached at De ≈ 1.75, before decaying as De continues to increase.

In addition to the primary flow (the Newtonian component, De $= 0$), elastic stresses around the snowman generate a secondary flow, understood simply as the difference between the total flow and the Newtonian component. A typical secondary flow pattern is shown in the frame of the snowman in Fig. 2(b) (De $= 0.1$ and $\zeta = 0.5$). We depict the velocity vectors and streamlines with the shaded/color map representing the flow speed. Fluid is drawn towards the snowman parallel to the equatorial plane and then expelled along the axis, while a ring vortex is detected in the front. The maximum speed of the secondary flow is observed at the rear of the snowman, only about 0.7% of the characteristic speed of the primary flow $R_L\Omega$.
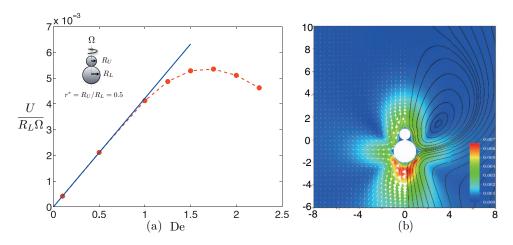
FIG. 2. Demonstration of snowman locomotion. In the case $r^* = R_U/R_L = 0.5$ and $\zeta = 0.5$, we plot: (a) dimensionless propulsion speed, $U/R_L\Omega$, as a function of the Deborah number, De. (Red dots and dashed line: numerical simulations in an Oldroyd-B fluid; blue solid line: theoretical calculation using the reciprocal theorem in a second-order fluid, Eq. (36).) (b) The streamline pattern and speed (shaded/color map) of the secondary flow for De $= 0.1$ (streamline patterns at higher De are qualitatively similar).

B. Small Deborah number

To provide a theoretical approach to the snowman locomotion and to quantify the connection between locomotion and rheology we now consider the second-order fluid, which we remind is valid in the small-De limit only (Eq. (11)). All variables are expanded in powers of the Deborah number, $\mathrm{De_{so}}$, as

$$\boldsymbol{\sigma} = \boldsymbol{\sigma}_0 + \mathrm{De_{so}}\boldsymbol{\sigma}_1 + O(\mathrm{De_{so}}^2), \tag{14}$$

$$\mathbf{u} = \mathbf{u}_0 + \mathrm{De_{so}}\mathbf{u}_1 + O(\mathrm{De_{so}}^2), \tag{15}$$

$$\dot{\boldsymbol{\gamma}} = \dot{\boldsymbol{\gamma}}_0 + \mathrm{De_{so}}\dot{\boldsymbol{\gamma}}_1 + O(\mathrm{De_{so}}^2), \tag{16}$$

$$\mathbf{U} = \mathbf{U}_0 + \mathrm{De_{so}}\mathbf{U}_1 + O(\mathrm{De_{so}}^2), \tag{17}$$

where $\mathbf{U}$ denotes the propulsion velocity, $\mathbf{U} = (0, 0, U)$. Other variables are expanded similarly. We drop the stars hereafter for simplicity, and all variables in this section are dimensionless unless otherwise stated. The locomotion problem is then solved order by order.

1. Zeroth-order solution

The zeroth-order solution, $\{\boldsymbol{\sigma}_0 = -p_0\mathbf{I} + \dot{\boldsymbol{\gamma}}_0, \mathbf{u}_0\}$, satisfies the Stokes equations,

$$\nabla \cdot \boldsymbol{\sigma}_0 = \mathbf{0}, \tag{18}$$

$$\nabla \cdot \mathbf{u}_0 = 0, \tag{19}$$

where $\boldsymbol{\sigma}_0 = -p_0\mathbf{I} + \dot{\boldsymbol{\gamma}}_0$. This is the Newtonian flow for two touching spheres rotating (at a rate of $\boldsymbol{\Omega}$) about the line of their centers (z-axis). The exact solution in terms of analytical functions was given by Takagi[61] in tangent-sphere coordinates. No propulsion occurs in the Newtonian limit, $\mathbf{U}_0 = \mathbf{0}$, as expected.

2. First-order solution

The first-order solution $(\boldsymbol{\sigma}_1, \mathbf{u}_1)$ of the main problem satisfies

$$\boldsymbol{\nabla} \cdot \boldsymbol{\sigma}_1 = \mathbf{0}, \tag{20}$$

$$\boldsymbol{\nabla} \cdot \mathbf{u}_1 = 0, \tag{21}$$

where

$$\boldsymbol{\sigma}_1 = -p_1 \mathbf{I} + \dot{\boldsymbol{\gamma}}_1 - \overset{\triangledown}{\dot{\boldsymbol{\gamma}}}_0 - B \dot{\boldsymbol{\gamma}}_0 \cdot \dot{\boldsymbol{\gamma}}_0. \tag{22}$$

To compute the value of the first-order propulsion velocity, $\mathbf{U}_1$, we will use a version of the reciprocal theorem for Stokes flows adapted to self-propulsion in viscoelastic fluids.[36, 46, 62–68]

Consider an auxiliary problem with identical geometry, $\{\boldsymbol{\sigma}_{\text{aux}}, \mathbf{u}_{\text{aux}}\}$, satisfying

$$\boldsymbol{\nabla} \cdot \boldsymbol{\sigma}_{\text{aux}} = \mathbf{0}, \tag{23}$$

$$\boldsymbol{\nabla} \cdot \mathbf{u}_{\text{aux}} = 0. \tag{24}$$

Taking the inner product of Eq. (20) with $\mathbf{u}_{\text{aux}}$, minus the inner product of Eq. (23) with $\mathbf{u}_1$, and integrating over the entire fluid volume, we have trivially

$$\int_{V_f} \mathbf{u}_{\text{aux}} \cdot (\boldsymbol{\nabla} \cdot \boldsymbol{\sigma}_1) - \mathbf{u}_1 \cdot (\boldsymbol{\nabla} \cdot \boldsymbol{\sigma}_{\text{aux}}) dV = 0. \tag{25}$$

Using vector calculus we can rewrite the integral in the following form:[69]

$$\int_{V_f} \boldsymbol{\nabla} \cdot (\mathbf{u}_{\text{aux}} \cdot \boldsymbol{\sigma}_1 - \mathbf{u}_1 \cdot \boldsymbol{\sigma}_{\text{aux}}) dV = \int_{V_f} (\boldsymbol{\nabla} \mathbf{u}_{\text{aux}} : \boldsymbol{\sigma}_1 - \boldsymbol{\nabla} \mathbf{u}_1 : \boldsymbol{\sigma}_{\text{aux}}) dV. \tag{26}$$

The left-hand side of Eq. (26) can be converted to a sum of surface integrals by the divergence theorem while the right-hand side can be simplified using the first-order constitutive equation, Eq. (22), leading to

$$\sum_\alpha \int_{S_\alpha} \mathbf{n} \cdot (\mathbf{u}_{\text{aux}} \cdot \boldsymbol{\sigma}_1 - \mathbf{u}_1 \cdot \boldsymbol{\sigma}_{\text{aux}}) dS = \int_{V_f} \left[\left(\overset{\triangledown}{\dot{\boldsymbol{\gamma}}}_0 + B \dot{\boldsymbol{\gamma}}_0 \cdot \dot{\boldsymbol{\gamma}}_0 \right) : \boldsymbol{\nabla} \mathbf{u}_{\text{aux}} \right] dV, \tag{27}$$

where S_α denotes the surface of different spheres ($\alpha = 1, 2$) and $\mathbf{n}$ represents the outward normal vector on the surface. The important simplification which took place in the right hand-side of Eq. (26) is that all Newtonian terms included in $\boldsymbol{\sigma}_{\text{aux}}$ and $\boldsymbol{\sigma}_1$ have canceled each other out by symmetry, and thus the only piece remaining in the right-hand side of Eq. (27) is the non-Newtonian contribution.[63, 68]

Now, let $\mathbf{U}_1$ and $\boldsymbol{\Omega}_1$ be the (unknown) first-order translational and rotational velocities of the spheres in our main problem, while the translational and rotational velocities of the spheres in the auxiliary problem (known) are given by $\mathbf{U}_{\text{aux}}$ and $\boldsymbol{\Omega}_{\text{aux}}$. On the surface S_α of one sphere, the no-slip and no-penetration boundary conditions lead to

$$\mathbf{u}_{\text{aux}} = \mathbf{U}_{\text{aux}} + \boldsymbol{\Omega}_{\text{aux}} \times \mathbf{r}, \tag{28}$$

$$\mathbf{u}_1 = \mathbf{U}_1 + \boldsymbol{\Omega}_1 \times \mathbf{r}, \tag{29}$$

where $\mathbf{r}$ is the position vector describing the surface. The integral relation, Eq. (27), becomes

$$\sum_\alpha \mathbf{U}_{\text{aux}}^\alpha \cdot \int_{S_\alpha} \mathbf{n} \cdot \boldsymbol{\sigma}_1 dS + \boldsymbol{\Omega}_{\text{aux}}^\alpha \cdot \int_{S_\alpha} \mathbf{r} \times (\mathbf{n} \cdot \boldsymbol{\sigma}_1) dS$$

$$-\mathbf{U}_1^\alpha \cdot \int_{S_\alpha} \mathbf{n} \cdot \boldsymbol{\sigma}_{\text{aux}} dS - \boldsymbol{\Omega}_1^\alpha \cdot \int_{S_\alpha} \mathbf{r} \times (\mathbf{n} \cdot \boldsymbol{\sigma}_{\text{aux}}) dS$$

$$= \int_{V_f} \left[\left(\overset{\triangledown}{\dot{\boldsymbol{\gamma}}}_0 + B \dot{\boldsymbol{\gamma}}_0 \cdot \dot{\boldsymbol{\gamma}}_0 \right) : \boldsymbol{\nabla} \mathbf{u}_{\text{aux}} \right] dV. \tag{30}$$

In Eq. (30), the integrals $\int_{S_\alpha} \mathbf{n} \cdot \boldsymbol{\sigma}_1 dS$ and $\int_{S_\alpha} \mathbf{r} \times (\mathbf{n} \cdot \boldsymbol{\sigma}_1) dS$ represent the net hydrodynamic force and torque acting on the sphere α by the first-order flow field. Let us denote $\mathbf{F}_1^\alpha = -\int_{S_\alpha} \mathbf{n} \cdot \boldsymbol{\sigma}_1 dS$ and $\mathbf{T}_1^\alpha = -\int_{S_\alpha} \mathbf{r} \times (\mathbf{n} \cdot \boldsymbol{\sigma}_1) dS$ the net external force ($\mathbf{F}_1^\alpha$) and external torque ($\mathbf{T}_1^\alpha$) acting on each sphere; the appearance of a minus sign comes from the fact that the total force and torque (external + fluid) acting on a body have to sum to zero in the absence of inertia. In the free-swimming case there is an additional stronger constraint, namely, the total external force (or equivalently, the total fluid force) has to remain zero at all instant (we will enforce this constraint shortly). Defining also $\mathbf{F}_{\text{aux}}^\alpha$ and $\mathbf{T}_{\text{aux}}^\alpha$ as the external force and torque required to balance the fluid drag and torque on each sphere in the auxiliary problem we see that Eq. (30) is transformed into

$$\sum_\alpha -\mathbf{U}_{\text{aux}}^\alpha \cdot \mathbf{F}_1^\alpha - \boldsymbol{\Omega}_{\text{aux}}^\alpha \cdot \mathbf{T}_1^\alpha + \mathbf{U}_1^\alpha \cdot \mathbf{F}_{\text{aux}}^\alpha + \boldsymbol{\Omega}_1^\alpha \cdot \mathbf{T}_{\text{aux}}^\alpha = \int_{V_f} \left[\left(\overset{\triangledown}{\dot{\boldsymbol{\gamma}}}_0 + B\dot{\boldsymbol{\gamma}}_0 \cdot \dot{\boldsymbol{\gamma}}_0 \right) : \boldsymbol{\nabla}\mathbf{u}_{\text{aux}} \right] dV. \quad (31)$$

The above relation remains actually true for any number of spheres and kinematics. In the case of a snowman, we have two spheres connected as a rigid body in both the main and auxiliary problems, hence $\mathbf{U}_1^1 = \mathbf{U}_1^2 = \mathbf{U}_1$, $\boldsymbol{\Omega}^1 = \boldsymbol{\Omega}^2 = \boldsymbol{\Omega}_1$, $\mathbf{U}_{\text{aux}}^1 = \mathbf{U}_{\text{aux}}^2 = \mathbf{U}_{\text{aux}}$, and $\boldsymbol{\Omega}_{\text{aux}}^1 = \boldsymbol{\Omega}_{\text{aux}}^2 = \boldsymbol{\Omega}_{\text{aux}}$. In the main problem we impose a rotational rate $\boldsymbol{\Omega}$ on the snowman, which has been accounted for in the zeroth-order (Newtonian) solution, hence $\boldsymbol{\Omega}_n^\alpha = \mathbf{0}$ for all $n \geq 1$. In addition, we define in the main problem the total external force and torque acting on the rigid body as $\mathbf{F}_1 = \mathbf{F}^1 + \mathbf{F}^2$ and $\mathbf{T}_1 = \mathbf{T}^1 + \mathbf{T}^2$, and in the auxiliary problem $\mathbf{F}_{\text{aux}} = \mathbf{F}_{\text{aux}}^1 + \mathbf{F}_{\text{aux}}^2$ and $\mathbf{T}_{\text{aux}} = \mathbf{T}_{\text{aux}}^1 + \mathbf{T}_{\text{aux}}^2$. Using these simplifications the general relation, Eq. (31), simplifies to

$$-(\mathbf{U}_{\text{aux}} \cdot \mathbf{F}_1 + \boldsymbol{\Omega}_{\text{aux}} \cdot \mathbf{T}_1) + \mathbf{U}_1 \cdot \mathbf{F}_{\text{aux}} = \int_{V_f} \left[\left(\overset{\triangledown}{\dot{\boldsymbol{\gamma}}}_0 + B\dot{\boldsymbol{\gamma}}_0 \cdot \dot{\boldsymbol{\gamma}}_0 \right) : \boldsymbol{\nabla}\mathbf{u}_{\text{aux}} \right] dV \cdot \quad (32)$$

We now need to find an auxiliary problem that facilitates the determination of the first-order propulsion velocity, $\mathbf{U}_1$, in the main problem. An appropriate candidate is the translation of two touching spheres along the line of their centers without rotation, $\boldsymbol{\Omega}_{\text{aux}} = \mathbf{0}$. The exact analytical solution was given by Cooley and O'Neill.[70] By choosing this auxiliary problem, the relation further simplifies to

$$-\mathbf{U}_{\text{aux}} \cdot \mathbf{F}_1 + \mathbf{U}_1 \cdot \mathbf{F}_{\text{aux}} = \int_{V_f} \left[\left(\overset{\triangledown}{\dot{\boldsymbol{\gamma}}}_0 + B\dot{\boldsymbol{\gamma}}_0 \cdot \dot{\boldsymbol{\gamma}}_0 \right) : \boldsymbol{\nabla}\mathbf{u}_{\text{aux}} \right] dV \cdot \quad (33)$$

If we do not allow the spheres to translate along the z-axis, $\mathbf{U}_1 = \mathbf{0}$, an external force, $\mathbf{F}_1$, is required to hold the snowman in place given by

$$-\mathbf{U}_{\text{aux}} \cdot \mathbf{F}_1 = \int_{V_f} \left[\left(\overset{\triangledown}{\dot{\boldsymbol{\gamma}}}_0 + B\dot{\boldsymbol{\gamma}}_0 \cdot \dot{\boldsymbol{\gamma}}_0 \right) : \boldsymbol{\nabla}\mathbf{u}_{\text{aux}} \right] dV \cdot \quad (34)$$

On the other hand, if we allow the snowman to translate freely without imposing any external forces, $\mathbf{F}_1 = \mathbf{0}$, then the first-order propulsion velocity, $\mathbf{U}_1$, can be determined from

$$\mathbf{U}_1 \cdot \mathbf{F}_{\text{aux}} = \int_{V_f} \left[\left(\overset{\triangledown}{\dot{\boldsymbol{\gamma}}}_0 + B\dot{\boldsymbol{\gamma}}_0 \cdot \dot{\boldsymbol{\gamma}}_0 \right) : \boldsymbol{\nabla}\mathbf{u}_{\text{aux}} \right] dV, \quad (35)$$

where both $\mathbf{F}_{\text{aux}}$ and the integral are expressed in terms of known Newtonian solutions of the main and auxiliary problems. Since the propulsion velocity $\mathbf{U}_1$ (with magnitude U_1) and the force in the auxiliary problem $\mathbf{F}_{\text{aux}}$ (with magnitude F_{aux}) act both vertically, the first-order propulsion speed is finally given by

$$U_1 = \frac{1}{F_{\text{aux}}} \int_{V_f} \left[\left(\overset{\triangledown}{\dot{\boldsymbol{\gamma}}}_0 + B\dot{\boldsymbol{\gamma}}_0 \cdot \dot{\boldsymbol{\gamma}}_0 \right) : \boldsymbol{\nabla}\mathbf{u}_{\text{aux}} \right] dV, \quad (36)$$

where a positive value represents upward propulsion.

Using Eq. (36) with the zeroth-order solution[61] and the auxiliary Newtonian solution[70] we are able to determine theoretically the leading order propulsion speed of the snowman, $U = \mathrm{De}_{\mathrm{so}} U_1 + O(\mathrm{De}_{\mathrm{so}}^2) = \mathrm{De}(1 - \zeta) U_1 + O(\mathrm{De}^2)$. The quadrature is performed in the tangent-sphere coordinates, with somewhat lengthy differential operations in evaluating the integrand. Our asymptotic results are shown in Fig. 2 as a blue solid line. We see that our results predict very well the propulsion speed of the snowman for small De when compared with numerical computations of the Oldroyd-B fluid (red dots and dashed line in Fig. 2), and the agreement is excellent up to De $\sim$ 1.

Note that in order to compare the results between the second-order fluid calculation and the Oldroyd-B numerics, the dimensionless parameter $B = -2\Psi_2/\Psi_1$ in the second-order fluid has to be taken to be zero because the second normals stress coefficient is zero in the Oldroyd-B model. Experimentally, indeed we have $B \ll 1$. Mathematically, the propulsion velocity varies linearly with B, and a transition of propulsion direction occurs at $B = 1$. Such a transition also occurs in the direction of radial flow for a single rotating sphere in a second-order fluid (see Sec. V for a related discussion).

C. Propulsion characteristics

Anticipating the section where we make the link between rheology and locomotion, we now investigate the impact of the snowman geometry on its propulsion performance in the low-De regime where our asymptotic results via reciprocal theorem are quantitatively accurate.

1. Touching spheres

In the case of two touching spheres ($h^* = 1 + r^*$), the only free dimensionless geometric parameter is the ratio of the radius of the upper to that of the lower spheres $r^* = R_U/R_L \in [0, 1]$. In the limit $r^* = 0$, the snowman reduces to a single sphere, while the limit $r^* = 1$ corresponds to two equal touching spheres; in both cases, there is no propulsion by symmetry. We therefore expect an optimal ratio r^* for a maximum propulsion speed. Using the reciprocal theorem, Eq. (36), we calculate the propulsion speed as a function of r^* (Fig. 3, blue solid line) and compare with the numerical results in an Oldroyd-B fluid (Fig. 3, red dots) at De = 0.1 and a typical relative viscosity $\zeta = 0.5$. The asymptotic results agree very well with the Oldroyd-B computations. The optimal sphere size ratio occurs at $r^*_{\mathrm{opt}} \approx 0.58$. In addition to our computations and theoretical calculations, and based on physical understanding of the behavior of a single rotating sphere in a second-order
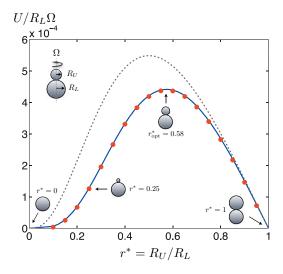

FIG. 3. Propulsion speed of snowman with two touching spheres as a function of the ratio of radii at De = 0.1 and $\zeta = 0.5$. Red dots: numerical results in an Odroyd-B fluid. Blue solid line: theoretical calculation for second-order fluid. Black dotted line: simplified analytical model (Eq. (51)).

fluid, a simplified analytical model can be constructed to predict the snowman dynamics with results shown as a black dotted line in Fig. 3; the details of this simple model are given in Sec. V.

2. Separated spheres

Next, we let the two spheres be separated at a distance $h^* > 1 + r^*$ (no longer touching). The two spheres still rotate at the same speed as a rigid body and the separation distance is kept fixed by connecting the spheres with a drag-less slender rigid rod (a mathematically phantom rod) with negligible hydrodynamic contribution. Experimentally, this may be realized, for example, using nanowires.[71] To compute the propulsion speed by the method described in Sec. III B 2 and therefore Eq. (36), we need two new Newtonian solutions, namely, the zeroth-order solution and the auxiliary problem. The zeroth-order solution considers two separated unequal spheres rotating at the same rate in a Newtonian fluid, the exact solution of which was given by Jeffery[72] in bi-spherical coordinates. The appropriate auxiliary problem is the translation in a Newtonian fluid of the same two-sphere geometry along their axis of symmetry. Stimson and Jeffery[73] calculated that exact solution also in bi-spherical coordinates.

For very separated spheres $h^* \gg 1$, the propulsion is expected to decay with the separation distance. Hydrodynamic interactions between the two spheres are weak in this limit and each sphere behaves approximately as a single rotating sphere which does not propel. In Fig. 4(a), the variation of the propulsion speed as a function of the separated distance is calculated for different fixed values of r^*. The propulsion speed decays as expected for large h^*. Interestingly, a non-monotonic variation occurs when the spheres are close to each other (small h^*). The swimming speed first increases with h^*, reaching a maximum around $h^* \approx 2.5$, before decaying to zero with further increase in h^*. In Sec. V, a simple physical explanation to this non-monotonicity is discussed; the black dotted line in Fig. 4(a) corresponds to the predictions by a simplified analytical model based on this explanation.

For separated spheres, we can again vary the radii ratio, r^*, at different fixed separated distances h^* (Fig. 4(b)) and results similar to the case of touching spheres are observed: for any value of h^* there exists an optimal value of r^* at which the dimensionless propulsion speed reaches a maximum. The simplified model (Sec. V) again captures this trend qualitatively (black dotted line, Fig. 4(b)).

Finally, by plotting the isovalues of the propulsion speed as a function of both r^* and h^* (Fig. 5), we are able to optimize the snowman geometry for the overall maximum propulsion speed. The optimal geometry occurs at $(r^*, h^*) = (0.46, 2.5)$, and a schematic diagram of the optimal snowman is drawn to-scale in Fig. 5.
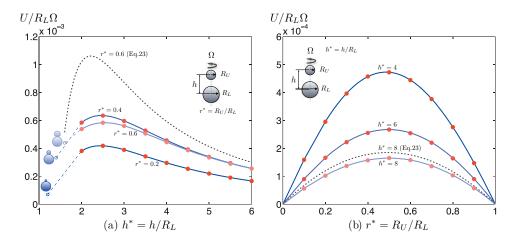

FIG. 4. Propulsion speed of a separated snowman as a function of (a) the separation distance, and (b) ratio of the radii, at De = 0.1 and ζ = 0.5. Red dots: numerical results in an Odroyd-B fluid. Blue solid line: second-order fluid analytical calculation. Black dotted line: simplified model (Eq. (50)).
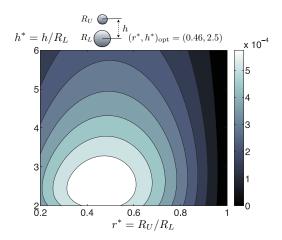
FIG. 5. Optimization snowman propulsion. Isovalues of the dimensionless propulsion speed with dimensionless separation distance, h^*, and ratio of sphere radii, r^*. The optimal geometry for maximum propulsion speed is given by $(r^*, h^*)_{\text{opt}}$ = (0.46, 2.5). A schematic diagram showing the optimal geometry is drawn to scale above.

IV. MICRORHEOLOGY VIA SNOWMAN

A. Scaling

In Sec. III B we have derived an analytical expression, valid in the small De regime, relating the propulsion speed to the intrinsic properties of the complex fluid, namely, the normal stress coefficients (Eq. (36)). Turning all dimensionless variables back in dimensional form, this relationship reads formally

$$U = \left(C_1^{\text{S}}\Psi_1 + C_2^{\text{S}}\Psi_2\right) \frac{R_L\Omega^2}{\eta}, \tag{37}$$

where C_1^{S} and C_2^{S} are dimensionless coefficients depending solely on the snowman geometry (h^* and r^*) and defined as

$$C_1^{\text{S}} = \frac{\int_{V_f^*} \overset{\triangledown}{\dot{\boldsymbol{\gamma}}_0^*} : \boldsymbol{\nabla}^* \mathbf{u}_{\text{aux}}^* dV^*}{2F_{\text{aux}}^*}, \tag{38}$$

$$C_2^{\text{S}} = -\frac{\int_{V_f^*} \left(\dot{\boldsymbol{\gamma}}_0^* \cdot \dot{\boldsymbol{\gamma}}_0^*\right) : \boldsymbol{\nabla}^* \mathbf{u}_{\text{aux}}^* dV^*}{F_{\text{aux}}^*}. \tag{39}$$

Since the second normal stress coefficient Ψ_2 is usually much smaller than the first normal stress coefficients Ψ_1, we might ignore Ψ_2 and obtain an estimation of Ψ_1 by measuring the propulsion speed of a snowman U, i.e.,

$$\Psi_1 \approx \frac{U}{C_1^{\text{S}}} \frac{\eta}{R_L\Omega^2}, \tag{40}$$

where C_1^{S} depends only on geometry and can be computed using Eq. (38). This expression demonstrates the use of locomotion (U) to probe the local non-Newtonian properties of the fluid (Ψ_1).

B. Second experiment: Repulsion of two equal spheres

In scenarios where both values of Ψ_1 and Ψ_2 are desired, a second experiment is necessary to obtain a second, independent, measurement of a combination of the normal stress coefficients. We propose to measure in the second experiment the relative speed (repulsion) of two rotating equal spheres of radius R_E, with their centers separated by a distance h (see Fig. 6 inset for notations and
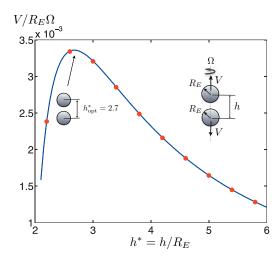
FIG. 6. Dimensionless repulsion speed, $V/R_E\Omega$, of two equal co-rotating spheres as a function of their dimensionless separation distance, h^*, at De $= 0.1$ and $\zeta = 0.5$. Red dots: numerical results in an Odroyd-B fluid. Blue solid line: theoretical calculation for a second-order fluid.

geometry). Should the two equal spheres be connected as a rigid body, no propulsion would occur by symmetry. However, if the equal spheres are not connected but allowed to freely translate along their separation axis, upon imposing rotation they will translate with velocities of equal magnitude but opposite directions provided the fluid is non-Newtonian.

We adopt the same non-dimensionalizations as Sec. II C (all lengths are now scaled by R_E) and drop the stars for simplicity; all variables in this section are dimensionless unless otherwise stated. Denoting the dimensionless velocity of the lower sphere as $\mathbf{V}$, we again expand the repulsion velocity in powers of $\mathrm{De_{so}}$, $\mathbf{V} = \mathrm{De_{so}}\mathbf{V}_1 + O(\mathrm{De_{so}}^2)$, and determine the first-order velocity $\mathbf{V}_1$ by our use of the reciprocal theorem as described in Sec. III B 2. By symmetry, the upper sphere translates with velocity $-\mathbf{V}$ (equal speed but opposite direction as the lower sphere).

In this scenario we have to again define two setups, one for the main problem and one for the auxiliary problem. For the main problem, we consider the rotational motion of two free equal spheres about their line of centers.[72] Since the motion is force-free ($\mathbf{F}_1^\alpha = \mathbf{0}$ at each instant), Eq. (36) simplifies to

$$-\mathbf{\Omega}_{\mathrm{aux}}^1 \cdot \mathbf{T}^1 - \mathbf{\Omega}_{\mathrm{aux}}^2 \cdot \mathbf{T}^2 + \mathbf{U}_1^1 \cdot \mathbf{F}_{\mathrm{aux}}^1 + \mathbf{U}_2^1 \cdot \mathbf{F}_{\mathrm{aux}}^2 = \int_{V_f}\left[\left(\overset{\triangledown}{\dot{\boldsymbol{\gamma}}}_0 + B\dot{\boldsymbol{\gamma}}_0 \cdot \dot{\boldsymbol{\gamma}}_0\right) : \boldsymbol{\nabla}\mathbf{u}_{\mathrm{aux}}\right]dV, \quad (41)$$

where $\mathbf{\Omega}_1^\alpha = \mathbf{0}$ for the same reason as explained in Sec. III B 2.

For the auxiliary problem, we consider the Newtonian translational motion ($\mathbf{\Omega}_{\mathrm{aux}}^\alpha = \mathbf{0}$) of two equal spheres moving towards each other at the same speed and hence force, $\mathbf{F}_{\mathrm{aux}}^1 = -\mathbf{F}_{\mathrm{aux}}^2 = \mathbf{F}_{\mathrm{aux}}^E$. The exact solution to this problem was found by Brenner[74] in bi-spherical coordinates. We therefore have

$$\left(\mathbf{U}_1^1 - \mathbf{U}_1^2\right) \cdot \mathbf{F}_{\mathrm{aux}}^E = \int_{V_f}\left[\left(\overset{\triangledown}{\dot{\boldsymbol{\gamma}}}_0 + B\dot{\boldsymbol{\gamma}}_0 \cdot \dot{\boldsymbol{\gamma}}_0\right) : \boldsymbol{\nabla}\mathbf{u}_{\mathrm{aux}}\right]dV. \quad (42)$$

Note that the main problem here is a special case of that considered in Sec. III B 2, but the auxiliary problem is completely different. We however still use the same symbols as in Sec. III B 2 for simplicity.

By symmetry, the two equal spheres propel with equal speed in opposite directions $\mathbf{U}_1^2 = -\mathbf{U}_1^1 = \mathbf{V}_1$, hence

$$-2\mathbf{V}_1 \cdot \mathbf{F}_{\mathrm{aux}}^E = \int_{V_f}\left[\left(\overset{\triangledown}{\dot{\boldsymbol{\gamma}}}_0 + B\dot{\boldsymbol{\gamma}}_0 \cdot \dot{\boldsymbol{\gamma}}_0\right) : \boldsymbol{\nabla}\mathbf{u}_{\mathrm{aux}}\right]dV. \quad (43)$$

Since the repulsion velocity $\mathbf{V}_1$ (with magnitude V_1) and the force in the auxiliary problem $\mathbf{F}_{\text{aux}}^E$ (with magnitude F_{aux}^E) both act vertically, the equation above can be rewritten as

$$V_1 = -\frac{1}{2F_{\text{aux}}^E} \int_{V_f} \left[\left(\overset{\triangledown}{\dot{\boldsymbol{\gamma}}}_0 + B\dot{\boldsymbol{\gamma}}_0 \cdot \dot{\boldsymbol{\gamma}}_0 \right) : \nabla \mathbf{u}_{\text{aux}} \right] dV, \tag{44}$$

where a positive value of V_1 represents repulsion.

The only dimensionless parameter in this second experiment is the ratio of the separation distance to the radius of the spheres, which we write as $h^* = h/R_L$. Using Eq. (44) we calculate the repulsion speed ($V_1 > 0$) as a function of the dimensionless separation h^* (blue solid line, Fig. 6, for De $= 0.1$ and $\zeta = 0.5$), and the results are found to be in excellent agreement with the Oldroyd-B calculations (red dots, Fig. 6).

Back to dimensional variables, the leading order repulsion speed is formally given by

$$V = \left(C_1^{\text{E}}\Psi_1 + C_2^{\text{E}}\Psi_2 \right) \frac{R_E \Omega^2}{\eta}, \tag{45}$$

where C_1^{E} and C_2^{E} are dimensionless coefficients evaluated with the solution to the main and auxiliary problems described above

$$C_1^{\text{E}} = -\frac{\int_{V_f^*} \overset{\triangledown}{\dot{\boldsymbol{\gamma}}}_0^* : \nabla^* \mathbf{u}_{\text{aux}}^* dV^*}{4F_{\text{aux}}^*}, \tag{46}$$

$$C_2^{\text{E}} = \frac{\int_{V_f^*} \left(\dot{\boldsymbol{\gamma}}_0^* \cdot \dot{\boldsymbol{\gamma}}_0^* \right) : \nabla^* \mathbf{u}_{\text{aux}}^* dV^*}{2F_{\text{aux}}^*}. \tag{47}$$

C. Determination of normal stress coefficients

From measuring both the propulsion speed U of a snowman (given by Eq. (37)) and repulsion speed V of the equal spheres (given by Eq. (45)), we now have enough information to deduce both the first and second normal stress coefficients (Ψ_1, Ψ_2). If we choose the same radius for the lower sphere in both experiments $R_E = R_L$ (we use R_L hereafter), we can write Eqs. (37) and (45) in a matrix form as

$$\begin{pmatrix} U \\ V \end{pmatrix} = \begin{pmatrix} C_1^{\text{S}} & C_2^{\text{S}} \\ C_1^{\text{E}} & C_2^{\text{E}} \end{pmatrix} \begin{pmatrix} \Psi_1 \\ \Psi_2 \end{pmatrix} \frac{R_L \Omega^2}{\eta}, \tag{48}$$

where we denote by $\mathbf{C}$ the matrix containing the dimensionless coefficients ($C_1^{\text{S}}, C_2^{\text{S}}, C_1^{\text{E}}, C_2^{\text{E}}$) in Eq. (48). The matrix $\mathbf{C}$ depends only on three geometric parameters, namely, the ratio of the radii of the spheres in the snowman ($r^* = R_U/R_L$), the dimensionless separation distance in the snowman ($h_{\text{S}}^* = h/R_L$) and that for the equal spheres in the second experiment ($h_{\text{E}}^* = h/R_E$). The coefficients of the matrix can be readily computed via Eqs. (38) and (39) and Eqs. (46) and (47), and thus the matrix in Eq. (48) can be inverted to obtain the values of Ψ_1 and Ψ_2.

For practical implementation of this microrheological technique, measurement errors in the velocity of the snowman are inevitable and depend on the specific equipment employed for tracking the motion of the probe. However, the geometry of the snowman can be designed so that Ψ_1 and Ψ_2 are insensitive to measurement errors in the velocities U and V. The condition number (CN) of the matrix $\mathbf{C}$ to be inverted represents the maximum amplification factor of the relative measurement errors. The maximum relative errors in the normal stress coefficients would be equal to the condition number multiplied by the maximum relative measurement error. A small condition number is therefore desired. Similarly to the study by Khair and Squires,[46] we now investigate the value of condition number as a function of the geometry. To simplify the parametric studies, we first adopt the same separation distance in the first and second experiments ($h_{\text{S}}^* = h_{\text{E}}^* = h^* = h/R_L$), and explore the dependence of the condition number on r^* and h^*, with results shown in Fig. 7(a). The condition number does not vary monotonically with the parameters, which implies that optimization
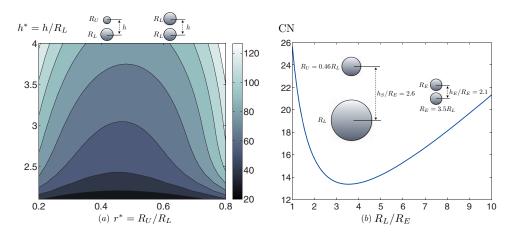
FIG. 7. (a) Condition number (CN) for the matrix **C** as a function of sphere size ratio (r^*) and dimensionless separation distance ($h^* = h_{\mathrm{S}}^* = h_{\mathrm{E}}^*$). (b) CN as a function of R_L/R_E, for $r^* = 0.46$, $h_{\mathrm{S}}^* = 2.6$, and $h_{\mathrm{E}}^* = 2.1$.

is possible. Under this requirement and within the ranges of values considered ($r^* \in [0.2, 0.98]$ and $h^* \in [2.1, 4]$), the geometry yielding the lowest condition number is $r^* = 0.46$ and $h^* = 2.1$ (the corresponding condition number for **C** is ≈ 27.6). When the requirement of $h_{\mathrm{S}}^* = h_{\mathrm{E}}^*$ is removed, by examining all combinations of the parametric values within the ranges ($r^* \in [0.2, 0.98]$, $h_{\mathrm{S}}^* \in [2.1, 4]$, and $h_{\mathrm{E}}^* \in [2.1, 4]$), the minimum CN obtainable appears to be ≈ 25.7 with $r^* = 0.46$, $h_{\mathrm{S}}^* = 2.6$, and $h_{\mathrm{E}}^* = 2.1$.

The condition number can be further fine-tuned if we allow $R_L \neq R_E$, in which case we have the new matrix relation:

$$\begin{pmatrix} U \\ V \end{pmatrix} = \begin{pmatrix} C_1^{\mathrm{S}} & C_2^{\mathrm{S}} \\ C_1^{\mathrm{E}} R_E/R_L & C_2^{\mathrm{E}} R_E/R_L \end{pmatrix} \begin{pmatrix} \Psi_1 \\ \Psi_2 \end{pmatrix} \frac{R_L \Omega^2}{\eta}. \tag{49}$$

The modified dimensionless matrix $\tilde{\mathbf{C}}$ in Eq. (49) now depends on one more parameter R_L/R_E, which is the ratio of the lower sphere radius in the snowman, R_L, to that of the equal sphere, R_E. In Fig. 7(b), we investigate the dependence of the condition number of $\tilde{\mathbf{C}}$ with this new parameter, and adopt for all other parameters the optimal geometric parameters we determined before ($r^* = 0.46$, $h_{\mathrm{S}}^* = 2.6$, and $h_{\mathrm{E}}^* = 2.1$). The variation turns out to be also non-monotonic, and a minimum is achieved when $R_L/R_E = 3.5$ with CN ≈ 13.4. A schematic diagram showing the corresponding geometrical setup of the two sets of experiment is given to scale in the inset of Fig. 7. The condition number could be brought further down with a full four-dimensional parametric study and expanding the domains of the parametric studies. However, geometries yielding a lower CN may correspond to a negligible speeds undesirable for measurement. The current geometry ($r^* = 0.46$, $h_{\mathrm{S}}^* = 2.6$, $h_{\mathrm{E}}^* = 2.1$, and $R_L/R_E = 3.5$) has both a relatively low CN and a high propulsion speed, making it ideal for experimental implementation. It is interesting to note that the optimal geometry for a small condition number we find here is close to the optimal geometry producing the maximum propulsion speed for the snowman ($r^* = 0.46$, $h_{\mathrm{S}}^* = 2.5$) determined in Sec. III C 2.

V. QUALITATIVE PHYSICAL EXPLANATION

In this section, we turn to an explanation of the physical origin of the non-Newtonian propulsion of a snowman. Based on physical intuition we present a simple model which successfully captures all the qualitative features of this mode of propulsion.

We first look into the simplest related problem, that of a single sphere rotating in a complex fluid (a textbook problem discussed, for example, in Ref. 9). Non-Newtonian stresses lead to the creation of a secondary flow in which the fluid moves towards the sphere in the equatorial plane
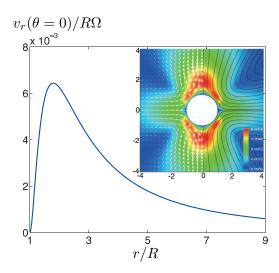
FIG. 8. Rotation of a single sphere in a second-order fluid. Radial velocity along the rotation axis ($\theta = 0$) as a function of r/R at De = 0.1 and $\zeta = 0.5$. (Inset) Streamline pattern and velocity (shaded/color map) of the corresponding secondary flow.

and away from the sphere near the axis of rotation (see the inset of Fig. 8 for an illustration of the secondary flow field).[9]

This secondary flow can be understood physically as a consequence of the hoop stresses along the curved streamlines. Polymer molecules in the fluid get stretched by the flow, leading to an extra tension along streamlines. The presence of that extra tension along the closed circular streamlines leads to an inward radial contraction (like a stretched rubber band) pushing the fluid to thus go up vertically in both directions (by continuity) to produce the secondary flow. Notably, this secondary flow is independent of the direction of rotation of the sphere.

The argument for locomotion of the snowman is then the following. Based on the one-sphere result, we see that when the two spheres in a snowman are aligned vertically and subject to a rotation they generate secondary flows and push against each other. For a single sphere, the strength of the secondary flow increases with the size of the sphere.[9] Consequently the smaller sphere is being pushed harder by the larger sphere than it is able to push against, and hence the two-sphere system is subject to a force imbalance, leading to propulsion. This physical understanding agrees with our results: propulsion always occurs in the direction of the smaller sphere, independently of the direction of rotation. Should the two spheres not be connected as a rigid body but free to translate vertically, they would repel each other, explaining physically our results in Sec. IV B.

Based on this intuitive argument, we can now construct a simple mathematical model. Using the same notations as above, for a sphere of radius R rotating with an angular velocity Ω in a second-order fluid, the leading order solution $\mathbf{v}(\phi, r, \theta)$ in spherical coordinates[9] is $\mathbf{v}^* \equiv \mathbf{v}/R\Omega = (1/r^*)^2 \sin\theta\, \hat{\mathbf{e}}_\phi + \mathrm{De}_{\mathrm{so}}(1 - B)[(1/2r^{*2} - 3/2r^{*4} + 1/r^{*5})(3\cos^2\theta - 1)\hat{\mathbf{e}}_r - 3(1/r^{*4} - 1/r^{*5})\sin\theta\cos\theta\,\hat{\mathbf{e}}_\theta] + O\left(\mathrm{De}_{\mathrm{so}}{}^2\right)$. The Newtonian component of the flow field ($\mathrm{De}_{\mathrm{so}} = 0$) is the primary flow field, and it has only a azimuthal (ϕ) component. The secondary flow field, proportional to $\mathrm{De}_{\mathrm{so}}$, is due to fluid elasticity and has only radial (r) and polar (θ) components. As expected, the dimensional secondary flow $\mathbf{v}$ is quadratic in Ω, confirming our physical intuition that it should be independent of the direction of rotation of the sphere. In the case where $B < 1$ (recall that $B = -2\Psi_2/\Psi_1$), the relevant limit for polymeric fluids, the secondary flow occurs in the direction intuited above and shown in the inset of Fig. 8. Note that the secondary flow field of a rotating single sphere would switch its direction when B went above one, explaining the switch in the propulsion direction of a snowman reported in Sec. III B 2 in that limit.

The dimensionless fluid velocity along the vertical axis ($\theta = 0$) is given by $\mathbf{v}^*(r, \theta = 0) = \mathrm{De}_{\mathrm{so}}\left(1/r^{*2} - 3/r^{*4} + 2/r^{*5}\right)\hat{\mathbf{e}}_r(\theta = 0)$, where we have set $B = 0$ to allow comparison with the numerical results. The velocity along the vertical axis, shown in Fig. 8, is expected to display non-monotonic variation with the distance from the sphere since the velocity decreases to zero both

in the far field and on the solid surface. This is at the origin of the non-monotonic dependence of the snowman propulsion speed with the separation distance between the spheres shown in Fig. 4(a).

The forces experienced by the upper and lower spheres can be approximately estimated by considering the individual flow fields generated by their own rotation without the presence of the other sphere. We place an upper sphere at a distance $h^* = h/R_L$ from the center of the lower sphere. Using the same notations as in the previous sections, the dimensionless velocity generated by the lower sphere, and evaluated at the location of the upper sphere, is given by $\mathbf{v}_L^*(h^*) = \mathrm{De}_{\mathrm{so}} \left(1/h^{*2} - 3/h^{*4} + 2h^{*5}\right) \hat{\mathbf{e}}_r^L(\theta^L = 0)$, where $\hat{\mathbf{e}}_r^L(\theta^L = 0)$ is the unit radial vector in the polar direction $\theta^L = 0$, with respect to the coordinates system at the center of the lower sphere. Similarly, the dimensionless velocity generated by the upper sphere at the same distance, h^*, but measured from the center of the upper sphere is given by $\mathbf{v}_U^*(h^*) = r^* \mathrm{De}_{\mathrm{so}} \left[(r^*/h^*)^2 - 3(r^*/h^*)^4 + 2(r^*/h^*)^5\right] \hat{\mathbf{e}}_r^U(\theta^U = \pi)$, where $\hat{\mathbf{e}}_r^U(\theta^U = \pi)$ is the unit radial vector in the polar direction $\theta^U = \pi$, with respect to the coordinates system at the center of the upper sphere. Note that $\hat{\mathbf{e}}_r^U(\theta^U = \pi) = -\hat{\mathbf{e}}_r^L(\theta^L = 0)$. As a simple approximation, we estimate the viscous drag force experienced by the upper and lower spheres to be $\mathbf{F}_U^* \sim 6\pi r^* \mathbf{v}_L^*(h^*)$ and $\mathbf{F}_L^* \sim 6\pi \mathbf{v}_U^*(h^*)$, respectively. The difference between these two forces results in a net propulsive thrust. When dividing by an approximation of the translational resistance of the snowman at zero Deborah number with no hydrodynamic interactions, $6\pi(1 + r^*)$, we obtain a simple estimate of the dimensionless propulsion speed as $U^* \approx |\mathbf{F}_U^* + \mathbf{F}_L^*|/6\pi(1 + r^*)$. This leads to

$$U^* \approx \frac{|r^* \mathbf{v}_L^*(h^*) + \mathbf{v}_U^*(h^*)|}{(1 + r^*)} = \mathrm{De}_{\mathrm{so}} \frac{r^* \left[3h^*(r^{*4} - 1) - h^{*3}(r^{*2} - 1) - 2r^{*5} + 2\right]}{h^{*5}(1 + r^*)}. \tag{50}$$

In Eq. (50), we verify that U^* vanishes when $r^* = 0$ (single sphere) and $r^* = 1$ (equal spheres). For the case of touching spheres ($h^* = 1 + r^*$), Eq. (50) simplifies to

$$U_{\mathrm{touch}}^* \approx \mathrm{De}_{\mathrm{so}} \frac{2r^{*3}(1 - r^*)}{(1 + r^*)^6}. \tag{51}$$

Does this simple model capture the essential propulsion characteristics? In Fig. 3, we plot the dimensionless propulsion speed of a touching snowman estimated by this simple model (Eq. (51)) as a function of r^* (black dotted line) and compare with the theoretical results from the reciprocal theorem approach (blue solid line) and the numerical computations (red symbols). The simple model correctly predicts the order of magnitude and captures qualitatively the variation with r^*. For non-touching snowman, the qualitative model (Eq. (50)) also captures qualitatively the variation of the dimensionless propulsion speed with h^* (dotted line for $r^* = 0.6$, Fig. 4(a)), predicting an optimal separation distance and therefore supporting our understanding of a non-monotonic dependence with h^* as arising from the non-monotonicity of the single-sphere velocity (Fig. 8). As expected, Eq. (50) also captures the non-monotonic variation with respect to r^* for separated snowman (dotted line for $h^* = 8$, Fig. 4(b)).

VI. DISCUSSION AND CONCLUSIONS

In this work, we present the design and mathematical modeling for a new non-Newtonian swimmer—the snowman—which propels only in complex fluids by exploiting asymmetry and the presence of normal stress differences under rotational actuation. The simple shape of our swimmer makes it ideally suited for experimental measurements. Note that if kept in place, the snowman would then act as a micro-pump for complex fluids.

The propulsion characteristics of the snowman are investigated by a combination of numerical computations (moderate values of De in an Odroyd-B fluid) and analytical treatment (small De in a second-order fluid). The underlying physics of propulsion, relying on elastic hoop stresses and geometrical asymmetry, is explained and based on this physical understanding a simple analytical model capturing all qualitative features is successfully constructed. Note that since, as a rule of thumb, inertial and elastic effects tend to produce secondary flows in opposite directions,[9] we expect that an inertial (instead of viscoelastic) snowman should swim in the opposite direction (from small to large sphere).

The two-sphere setup proposed in this work is arguably the simplest geometry able to swim in a complex fluid under uniform rotation. It of course simplifies the analysis since the required Newtonian solutions to be used in our integral approach are all available. Any axisymmetric but top-down asymmetric geometry should also work, for example, a cone, and clearly there remains room for shape optimization in that regard. Additionally, studying the snowman dynamics under a time-varying rotation could lead to a rich dynamics with potentially non-trivial stress relaxation effects.

One of the main ideas put forward in this work is the use of locomotion as a proxy to probe the local non-Newtonian properties of the fluid. The snowman can be used as a micro-rheometer to estimate the first normal stress coefficient on its own, or to measure both the first and second normal stress coefficients with the help of another complementary experiment. Khair and Squires[46] recently proposed to measure normal stress coefficients by pulling microrheological probes and measuring the relative forces on the probes. In our work, we propose alternatively to perform only kinematic measurements of the sphere speeds instead of forces, which could present an interesting alternative from an experimental standpoint.

We finally comment on a potential experimental implementation of the snowman technique. We are aware of a number of rotational micro-manipulation techniques (see a short review in Ref. [75]). For example, spinning micro-particles may be achieved by the use of optical tweezers and birefringent objects.[76] Birefringence allows the transfer of angular momentum from the circularly polarized laser to the particle, producing controlled rotation. By rotating spherical birefringent crystals (vaterite), this technology has been implemented as a micro-viscometer to probe fluid viscosity.[75,77,78] A similar mechanism may be useful for the two-sphere setup in this work although simultaneous rotation of two spheres may introduce experimental challenges. Our dual-purpose snowman, both a micro-propeller and a micro-rheometer, invites experimental implementation and verification.

ACKNOWLEDGMENTS

[1] E. M. Purcell, "Life at low Reynolds number," Am. J. Phys. **45**, 3–11 (1977).

[2] C. Brennen and H. Winet, "Fluid mechanics of propulsion by cilia and flagella," Annu. Rev. Fluid Mech. **9**, 339–398 (1977).

[3] L. J. Fauci and R. Dillon, "Biofluidmechanics of reproduction," Annu. Rev. Fluid Mech. **38**, 371–394 (2006).

[4] E. Lauga and T. Powers, "The hydrodynamics of swimming microorganisms," Rep. Prog. Phys. **72**, 096601 (2009).

[5] R. Dreyfus, J. Baudry, M. L. Roper, M. Fermigier, H. A. Stone, and J. Bibette, "Microscopic artificial swimmsers," Nature (London) **437**, 862–865 (2005).

[6] J. Wang, "Can man-made nanomachines compete with nature biomotors?" ACS Nano **3**, 4–9 (2009).

[7] S. J. Ebbens and J. R. Howse, "In pursuit of propulsion at the nanoscale," Soft Matter **6**, 726–738 (2010).

[8] E. Lauga, "Life around the scallop theorem," Soft Matter **7**, 3060–3065 (2011).

[9] R. B. Bird, R. C. Armstrong, and O. Hassager, *Dynamics of Polymeric Liquids*, 2nd ed. (Wiley-Interscience, New York, 1987), Vol. 1.

[10] R. G. Larson, *The Structure and Rheology of Complex Fluids* (Oxford University Press, New York, NY, 1999).

[11] F. A. Morrison, *Understanding Rheology* (Oxford University Press, New York, NY, 2001).

[12] D. F. Katz, R. N. Mills, and T. R. Pritchett, "The movement of human spermatozoa in cervical mucus," J. Reprod. Fertil. **53**, 259–265 (1978).

[13] D. F. Katz and A. A. Berger, "Flagellar propulsion of human-sperm in cervical-mucus," Biorheology **17**, 169–175 (1980).

[14] D. F. Katz, T. D. Bloom, and R. H. Bondurant, "Movement of bull spermatozoa in cervical mucus," Biol. Reprod. **25**, 931–937 (1981).

[15] S. S. Suarez and X. Dai, "Hyperactivation enhances mouse sperm capacity for penetrating viscoelastic media," Biol. Reprod. **46**, 686–691 (1992).

[16] S. S. Suarez and A. A. Pacey, "Sperm transport in the female reproductive tract," Hum. Reprod. Update **12**, 23–37 (2006).

[17] M. A. Sleigh, J. R. Blake, and N. Liron, "The propulsion of mucus by cilia," Am. Rev. Respir. Dis. **137**, 726–741 (1988).

[18] C. Montecucco and R. Rappuoli, "Living dangerously: How helicobacter pylori survives in the human stomach," Nat. Rev. Mol. Cell Biol. **2**, 457–466 (2001).

[19] C. W. Wolgemuth, N. W. Charon, S. F. Goldstein, and R. E. Goldstein, "The flagellar cytoskeleton of the spirochetes," J. Mol. Microbiol. Biotechnol. **11**, 221–227 (2006).

[20] G. O'Toole, H. B. Kaplan, and R. Kolter, "Biofilm formation as microbial development," Annu. Rev. Microbiol. **54**, 49–79 (2000).

[21] R. M. Donlan and J. W. Costerton, "Biofilms: Survival mechanisms of clinically relevant microorganisms," Clin. Microbiol. Rev. **15**, 167–193 (2002).

[22] J. W. Costerton, K. J. Cheng, G. G. Geesey, T. I. Ladd, J. C. Nickel, M. Dasgupta, and T. J. Marrie, "Bacterial biofilms in nature and disease," Annu. Rev. Microbiol. **41**, 435–464 (1987).

[23] J. W. Costerton, Z. Lewandowski, D. E. Caldwell, D. R. Korber, and H. M. Lappin-Scott, "Microbial biofilms," Annu. Rev. Microbiol. **49**, 711–745 (1995).

[24] J. N. Wilking, T. E. Angelini, A. Seminara, M. P. Brenner, and D. A. Weitz, "Biofilms as complex fluids," MRS Bull. **36**, 385–391 (2011).

[25] R. B. Bird, C. F. Curtiss, R. C. Armstrong, and O. Hassager, *Dynamics of Polymeric Liquids*, 2nd ed. (Wiley-Interscience, New York, NY, 1987), Vol. 2.

[26] S. Ishijima, S. Oshio, and H. Mohri, "Flagellar movement of human spermatozoa," Gamete Res. **13**, 185 (1986).

[27] H. C. Fu, C. W. Wolgemuth, and T. R. Powers, "Beating patterns of filaments in viscoelastic fluids," Phys. Rev. E **78**, 041913 (2008).

[28] M. W. Harman, S. M. Dunham-Ems, M. J. Caimano, A. A. Belperron, L. K. Bockenstedt, H. C. Fu, J. D. Radolf, and C. W. Wolgemuth, "The heterogeneous motility of the lyme disease spirochete in gelatin mimics dissemination through tissue," Proc. Natl. Acad. Sci. U.S.A. **109**, 3059–3064 (2012).

[29] E. Lauga, "Propulsion in a viscoelastic fluid," Phys. Fluids **19**, 083104 (2007).

[30] H. C. Fu, T. R. Powers, and C. W. Wolgemuth, "Theory of swimming filaments in viscoelastic media," Phys. Rev. Lett. **99**, 258101 (2007).

[31] H. C. Fu, C. W. Wolgemuth, and T. R. Powers, "Swimming speeds of filaments in nonlinearly viscoelastic fluids," Phys. Fluids **21**, 033102 (2009).

[32] J. Teran, L. Fauci, and M. Shelley, "Viscoelastic fluid response can increase the speed and efficiency of a free swimmer," Phys. Rev. Lett. **104**, 038101 (2010).

[33] X. N. Shen and P. E. Arratia, "Undulatory swimming in viscoelastic fluids," Phys. Rev. Lett. **106**, 208101 (2011).

[34] B. Liu, T. R. Powers, and K. S. Breuer, "Force-free swimming of a model helical flagellum in viscoelastic fluids," Proc. Natl. Acad. Sci. U.S.A. **108**, 19516–19520 (2011).

[35] T. Normand and E. Lauga, "Flapping motion and force generation in a viscoelastic fluid," Phys. Rev. E **78**, 061907 (2008).

[36] E. Lauga, "Life at high Deborah number," Europhys. Lett. **86**, 64001 (2009).

[37] O. S. Pak, T. Normand, and E. Lauga, "Pumping by flapping in a viscoelastic fluid," Phys. Rev. E **81**, 036312 (2010).

[38] G. J. Elfring, O. S. Pak, and E. Lauga, "Two-dimensional flagellar synchronization in viscoelastic fluids," J. Fluid Mech. **646**, 505–515 (2010).

[39] A. Wineman and A. Pipkin, "Slow viscoelastic flow in tilted troughs," Acta Mech. **2**, 104–115 (1966).

[40] R. I. Tanner, "Some methods for estimating the normal stress functions in viscometric flows," Trans. Soc. Rheol. **14**, 483–507 (1970).

[41] E. Couturier, F. Boyer, O. Pouliquen, and E. Guazzelli, "Suspensions in a tilted trough: Second normal stress difference," J. Fluid Mech. **686**, 26–39 (2011).

[42] E. E. Brown, W. R. Burghardt, H. Kahvand, and D. C. Venerus, "Comparison of optical and mechanical measurements of second normal stress difference relaxation following step strain," Rheol. Acta **34**, 221–234 (1995).

[43] S. G. Baek and J. J. Magda, "Monolithic rheometer plate fabricated using silicon micromachining technology and containing miniature pressure sensors for N_1 and N_2 measurements," J. Rheol. **47**, 1249–1260 (2003).

[44] A. Kulkarni, S. Kharchenko, and R. Kannan, "Rheo-optical measurements of the first and third normal stresses of homopolymer poly(vinyl methyl ether) melt," Rheol. Acta **45**, 951–958 (2006).

[45] T. Schweizer, "Measurement of the first and second normal stress differences in a polystyrene melt with a cone and partitioned plate tool," Rheol. Acta **41**, 337–344 (2002).

[46] A. S. Khair and T. M. Squires, "Active microrheology: A proposed technique to measure normal stress coefficients of complex fluids," Phys. Rev. Lett. **105**, 156001 (2010).

[47] T. M. Squires and T. G. Mason, "Fluid mechanics of microrheology," Annu. Rev. Fluid Mech. **42**, 413–438 (2010).

[48] T. A. Waigh, "Microrheology of complex fluids," Rep. Prog. Phys. **68**, 685 (2005).

[49] D. Weihs, T. G. Mason, and M. A. Teitell, "Bio-microrheology: A frontier in microrheology," Biophys. J. **91**, 4296–4305 (2006).

[50] D. Wirtz, "Particle-tracking microrheology of living cells: Principles and applications," Annu. Rev. Biophys. **38**, 301–326 (2009).

[51] T. M. Squires, "Nonlinear microrheology: Bulk stresses versus direct interactions," Langmuir **24**, 1147–1159 (2008).

[52] E. F. Lee, D. L. Koch, and Y. L. Joo, "Cross-stream forces and velocities of fixed and freely suspended particles in viscoelastic poiseuille flow: Perturbation and numerical analyses," J. Non-Newtonian Fluid **165**, 1309–1327 (2010).

[53] R. Guénette and M. Fortin, "A new mixed finite element method for computing viscoelastic flows," J. Non-Newtonian Fluid Mech. **60**, 27–52 (1995).

[54] A. W. Liu, D. E. Bornside, R. C. Armstrong, and R. A. Brown, "Viscoelastic flow of polymer solutions around a periodic, linear array of cylinders: Comparisons of predictions for microstructure and flow fields," J. Non-Newtonian Fluid Mech. **77**, 153–190 (1998).

[55] J. Sun, M. D. Smith, R. C. Armstrong, and R. A. Brown, "Finite element method for viscoelastic flows based on the discrete adaptive viscoelastic stress splitting and the discontinuous Galerkin method: DAVSS-G/DG," J. Non-Newtonian Fluid Mech. **86**, 281–307 (1999).

[56] J. M. Marchal and M. J. Crochet, "A new mixed finite element for calculating viscoelastic flow," J. Non-Newtonian Fluid Mech. **26**, 77–114 (1987).

[57] L. Zhu, E. Lauga, and L. Brandt, "Self-propulsion in viscoelastic fluids: Pushers vs. pullers," Phys. Fluids **24**, 051902 (2012).

[58] F. P. T. Baaijens, "Mixed finite element methods for viscoelastic flow analysis: A review," J. Non-Newtonian Fluid Mech. **79**, 361–385 (1998).

[59] K. Walters and M. F. Webster, "The distinctive CFD challenges of computational rheology," Int. J. Numer. Methods Fluids **43**, 577–596 (2003).

[60] W. Lunsmann, L. Genieser, R. Armstrong, and R. Brown, "Finite element analysis of steady viscoelastic flow around a sphere in a tube: Calculations with constant viscosity models," J. Non-Newtonian Fluid Mech. **48**, 63–99 (1993).

[61] H. Takagi, "Slow rotation of two touching spheres in viscous fluid," J. Phys. Soc. Jpn. **36**, 875–877 (1974).

[62] B. P. Ho and L. G. Leal, "Migration of rigid spheres in a two-dimensional unidirectional shear flow of a second-order fluid," J. Fluid Mech. **76**, 783–799 (2010).

[63] B. Chan, N. J. Balmforth, and A. E. Hosoi, "Building a better snail: Lubrication and adhesive locomotion," Phys. Fluids **17**, 113101 (2005).

[64] P. Brunn, "The slow motion of a sphere in a second-order fluid," Rheol. Acta **15**, 163–171 (1976).

[65] P. Brunn, "The behavior of a sphere in non-homogeneous flows of a viscoelastic fluid," Rheol. Acta **15**, 589–611 (1976).

[66] L. G. Leal, "The slow motion of slender rod-like particles in a second-order fluid," J. Fluid Mech. **69**, 305–337 (1975).

[67] L. G. Leal, "Particle motions in a viscous fluid," Annu. Rev. Fluid Mech. **12**, 435–476 (1980).

[68] R. J. Phillips, "Dynamic simulation of hydrodynamically interacting spheres in a quiescent second-order fluid," J. Fluid Mech. **315**, 345–365 (1996).

[69] L. G. Leal, *Advanced Transport Phenomena: Fluid Mechanics and Convective Transport Processes* (Cambridge University Press, New York, 2007).

[70] M. B. A. Cooley and M. E. O'Neill, "On the slow motion of two spheres in contact along their line of centres through a viscous fluid," Math. Proc. Cambridge Philos. Soc. **66**, 407–415 (1969).

[71] If the drag on the slender rod is taken into account in modeling, the overall force balance should include the small contribution from the drag on the rod, which will slightly decrease the propulsion speed of the snowman.

[72] G. B. Jeffery, "On the steady rotation of a solid of revolution in a viscous fluid," Proc. London Math. Soc. (2) **14**, 327–338 (1915).

[73] M. Stimson and G. B. Jeffery, "The motion of two spheres in a viscous fluid," Proc. R. Soc. London, Ser. A **111**, 110–116 (1926).

[74] H. Brenner, "The slow motion of a sphere through a viscous fluid towards a plane surface," Chem. Eng. Sci. **16**, 242–251 (1961).

[75] A. I. Bishop, T. A. Nieminen, N. R. Heckenberg, and H. Rubinsztein-Dunlop, "Optical microrheology using rotating laser-trapped particles," Phys. Rev. Lett. **92**, 198104 (2004).

[76] M. E. J. Friese, T. A. Nieminen, N. R. Heckenberg, and H. Rubinsztein-Dunlop, "Optical alignment and spinning of laser-trapped microscopic particles," Nature (London) **394**, 348–350 (1998).

[77] G. Knöner, S. Parkin, N. R. Heckenberg, and H. Rubinsztein-Dunlop, "Characterization of optically driven fluid stress fields with optical tweezers," Phys. Rev. E **72**, 031507 (2005).

[78] S. J. Parkin, G. Knöner, T. A. Nieminen, N. R. Heckenberg, and H. Rubinsztein-Dunlop, "Picoliter viscometry using optically rotated particles," Phys. Rev. E **76**, 041507 (2007).